IEEE Access
Multidisciplinary ⋮ Rapid Review ⋮ Open Access Journal

Received 5 October 2024, accepted 29 October 2024, date of publication 4 November 2024, date of current version 12 November 2024.

Digital Object Identifier 10.1109/ACCESS.2024.3489801

RESEARCH ARTICLE

Laser-Induced Graphene RF Tags for Authentication Applications

ANTONIO LAZARO, (Senior Member, IEEE), MARCO RODRIGO CUJILEMA, FOAD SALEHNIA, RAMON VILLARINO, MARC LAZARO, AND DAVID GIRBAU, (Senior Member, IEEE)

Department of Electronics, Electrics and Automatic Control Engineering, Rovira i Virgili University, 43007 Tarragona, Spain

Corresponding author: Antonio Lazaro (antonioramon.lazaro@urv.cat)

This work was supported in part by Ministerio de Ciencia, Innovación y Universidades (MICIU)/Agencia Estatal de Investigación (AEI)/10.13039/501100011033/Fondo Europeo de Desarrollo Regional (FEDER), European Union (UE) under Grant PID2021-122399OB-I00; in part by MICIU/AEI/10.13039/501100011033/European Union NextGenerationEU/Plan de Recuperación, Transformación y Resiliencia (PRTR) under Grant TED2021-130307B-I00; and in part by under Grant PRE2019-089028 and Grant PRE2022-103744.

ABSTRACT With the rapid growth of online transactions, there has been a significant increase in fraud involving pharmaceuticals, textiles, and food, among others. This work proposes the use of non-cloneable authentication tags for product brand protection, in which both the type of substrate used and its geometry are combined, resulting in a unique spectral response. These tags are manufactured in two phases, a first one that forms a laser-induced graphene (LIG) layer, and a second one, based on an electroplating process, which produces traces with variable sheet resistance depending on the manufacturing parameters. This technology can be carried out using a common laser (e.g. CO_2 laser) to directly convert various precursors (e.g. polyimide) into graphene materials. A prototype scanner designed to characterize the electromagnetic signature of the tags is presented. Preliminary results obtained with simple resonators and complex images show the feasibility of this technology.

INDEX TERMS Radio identification, laser-induced graphene (LIG), chipless-RFID, ring resonator, near-field sensor, unclonable tag, authentication, counterfeit.

I. INTRODUCTION

In the context of a global market, authentication is necessary to combat counterfeit goods. This is especially interesting in large markets such as pharmaceuticals [1], [2], [3], [4], wines [5] or textiles [6], [7], [8]. Numerous anticounterfeit technologies have been documented in the literature for this purpose. One of these technologies is the use of fingerprints to develop physical unclonable functions (PUFs) [9]. Authentication differs from identification in that it not only identifies the object but also verifies its genuineness. Conventional passive radio frequency identification (RFID) has been proposed in [10] as an authentication solution. However, conventional RFID tags can be easily cloned. Therefore, the security level is not suitable for most applications. One possible solution is to design tags with a specific radio frequency fingerprint that contains a high level of randomness, which is, therefore, difficult to copy. In several works, some specific RF fingerprints for conventional RFID tags have been proposed. For instance, in [11], the threshold power of the tags has been employed, while [12] proposes a wavelet-based fingerprint. The backscattering response of nanostructure composite materials, the phase response of the backscattered signals, and the spectrum of their harmonics are studied in [13], [14], and [15], respectively. Chipless RFID technology refers to systems or methods that allow identification, tracking, and data transmission without the need for silicon-based microchips [16]. Unlike conventional RFID, chipless RFID tags rely on alternative methods to encode information. Two of these methods are based on obtaining the spectral signature (frequency coded chipless RFID [16], [17]) or on time-domain reflectometry (time-coded chipless RFID [18]). In addition to identification applications, chipless RFID has also been used for sensor development [19], [20]. By incorporating unique identifiers, chipless RFID can also help to verify the authenticity

The associate editor coordinating the review of this manuscript and approving it for publication was Huamin Li.

of products, thus combating counterfeiting. Authentication tags based on chipless RFID have already been proposed in previous works. For example, a chipless tag based on dipoles has been proposed in [21] and [22]. The randomness in the manufacturing of coupled C-folded resonators has been proposed in [23]. A tag with concentring ring slot resonators has been proposed as unclonable chipless RFID in [24]. Other chipless tags are based on the insertion of random wires inside a dielectric sealant that produces an RF fingerprint [25]. A similar concept using additive manufacturing has been recently presented in [26]. Most chipless tags for authentication are designed to be read in far field, although the reading range is typically limited to a few tens of cm. However, the use of chipless tags based on resonators that are read in near field has also been proposed [27]. Recently, multifunctional graphene has been recognized as a promising material for sensor manufacturing because of its exceptional mechanical, electrical, and thermal properties, as well as being a biocompatible material [28], [29], [30]. The two main techniques for the production of monolayer graphene are based on chemical vapor deposition or on the evaporation of a graphene solution [29]. However, these techniques are expensive and not suitable for industry production [29]. In 2014, a novel method for the fabrication of multifunctional 3D graphene known as laser-induced graphene (LIG) technology was proposed [31]. This method is based on the use of a common laser (eg. CO_2 laser) to directly convert various precursors into graphene (eg. polyimide), under ambient conditions of temperature and pressure [32]. The technique consists of writing with a laser on polyimide. LIG technology has emerged as a prominent approach for creating graphene-based sensors [29] such as piezoresistive transducers [33], capacitive strain sensors [34], biosensors [35], humidity sensors [36], and gas sensors [37].

The motivation of this work is to develop a novel technique for fabricating non-clonable tags with specific electromagnetic signatures for product authentication, thereby preventing counterfeiting. The EM signature is read in the near field using an innovative and straightforward scanning system. To this end, it is proposed the use of resonators made with LIG. The sheet resistivity of the substrate after printing the LIG traces depends mainly on the laser power and the printer speed, but also on the direction of the printed trace. However, the sheet resistivity that is obtained is too high, which results in a low-quality factor of the resonators. This quality factor is improved in a second step by the deposition of a metal layer of variable thickness (e.g. nickel) by electrolysis. To increase the difficulty of cloning, logo images are used as resonators. The main novelty of this work is the increase in the number of parameters that insert the randomness in the manufacturing of the tag, not only using the geometric tolerances but using the parameters of the manufacturing process itself, based on printing laser-induced graphene and electroplating, resulting in a device difficult to clone. The measurement of tag resonances is performed with a vector network analyzer (VNA) connected to a substrate-printed transmission line that is moved by a stepper motor, in order to scan the surface of the tag.

The remaining sections of this paper are organized as follows. Section II describes the proposed technology based on LIG. The design and implementation of the tags, and the influence of the manufacturing parameters are described in Section II-A. The electroplating procedure is described in II-A2. To characterize the performance of the conductive strips, measurements of quality factor of ring resonators are presented in section III-A. The prototype of scanner and experimental results of the tags are given in section III-B. Finally, a comparison with other solutions is provided in Section IV, and the main conclusions are highlighted in Section V.

II. SYSTEM OVERVIEW

A block diagram of the system is shown in Fig. 1. The tag is based on resonators embedded within an image of LIG directly printed with a CO_2 laser. The layout dimensions, shape and materials determine the resonance frequencies and frequency response. Depending on the laser manufacturing parameters the LIG conductivity and thickness change. In addition, to add more uncertainty to the result, a conductive layer with variable thickness is deposited on top of the LIG by electroplating. The characterization is based on a scanner. The transmission coefficient (S_{21} parameter) is characterized with a vector network analyzer using a setup which consists of a microstrip line connected to two SMA launch connectors at its ends, that is moved scanning the tag. The measured S_{21} parameter for each tag is saved in a database for later application of a validation procedure. This validation involves performing the measurement using the same configuration and comparing the tag's response with the one stored in the database. In the event of no coincidence, the tag is counterfeit. The manufacturing process is described below.

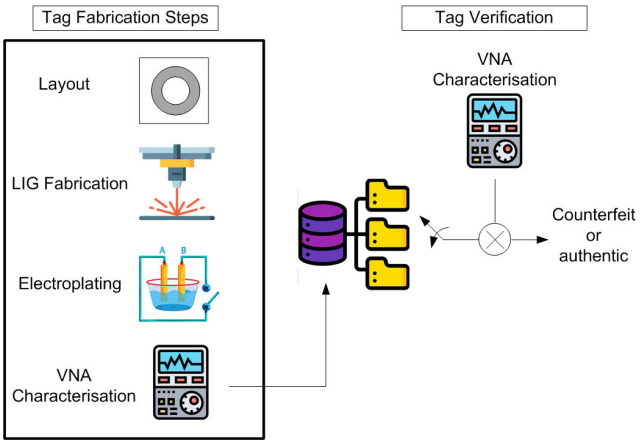

FIGURE 1. Block diagram of the proposed system.

A. TAG FABRICATION

The fabrication procedure includes the following steps: 1–layout definition, 2–LIG fabrication, 3–electroplating, and 4–characterisation.

1) LIG FABRICATION

The process starts with the precursor substrate selection, usually a polymer such as polyimide (PI). Polyimide (PI) films are readily available on the market and are widely employed to produce flexible electronics. Polyimide is commonly used due to its high carbon content and thermal stability. However, other carbon-rich polymers can also be used such as polyether ether ketone (PEEK) [38], poly(etherimide) (PEI) [39], various polysulfones (PSU) [40], and lignin [41]. In this work, the substrate selected is Kapton Dupont flexible polyimide with thickness 75 μm and dielectric permittivity $\epsilon_r = 3.4$. In the first step the substrate is cleaned with acetone and then attached to a polyethylene sheet with double-sided adhesive tape to avoid that the Kapton shrivels due to the temperature. This involves a later washing with solvents or other cleaning agents to remove contaminants. A FLUX Beambox 40W CO_2 laser engraver and cutter with a wavelength of 10.6 μm and a maximum power of 40 W is used for manufacturing. The resolution of the laser is 1000 dpi and the beamwidth is 50 μm. The laser beam is scanned over the substrate at a speed of 120-200 mm/s, and with a laser power level of 16-22%. A burning of the polyimide happens for larger powers than the aforementioned value in the range of scan speeds used. This precise scanning process allows the selective conversion of the polyimide film into graphene, thus patterning the desired figures, in this case, a resonator. The laser's high energy causes rapid localized heating of the polymer, reaching temperatures high enough to break the polymer chains. This process, known as photothermal conversion, transforms the carbon in the polymer into graphene. By controlling the laser's power, speed, and focus, the process can be precisely controlled to create specific patterns of graphene. The laser's parameters are adjusted to optimize graphene quality and properties, such as conductivity and layer thickness. The two main laser engraver parameters are its power and its scan speed. The graphene produced is characterized using techniques such as Raman spectroscopy. Table 1 shows the measured sheet resistance and Raman spectrum peak ratios of 4 samples with different parameters. The samples are strips 2 mm wide and 10 mm long. Fig. 2 shows the normalized intensity of the measured Raman shift spectrum for the 4 samples using an excitation laser wavelength of 514 nm. The Raman spectrum exhibits the characteristic peaks of graphitic structures at 1350 cm^{-1} (D peak) and 1585 cm^{-1} (G peak). The ratio between the first two peaks I_D/I_G permits to characterize the level of disorder existing in graphene [42], [43]. A strong D peak is an indicator of high defect concentration associated with defective graphene. From the measurements of the Raman spectrum, an I_D/I_G ratio of less than unity is obtained, with a relatively large width of the D peaks, which is indicative of the presence of graphitic porous structures [44].The ratio between 2D and G peaks is an indicator of the number of graphene layers. The strong 2D peak shows that the polyimide has been successfully converted to graphene with a small number of graphene layers [42], [43]. Both the ratio between the first two peaks I_D/I_G and the ratio between 2D and G peaks (I_{2D}/I_G) are also shown in Table 1. Fig. 3 shows the sheet resistance and the ratio between the 2D and G peaks as a function of energy per unit length. This energy is computed (and listed in Table 1) as the laser power by the scan speed. The result is the energy applied by unit length to the precursor substrate. This energy is proportional to both the heat and the amount of graphene induced, which is measured with the ratio I_{2D}/I_G. A linear behavior is found between the sheet resistance and the energy applied per unit length. Another technique proposed in the literature to reduce the sheet resistance is to defocus the laser beam [45], [46]. In this case, the laser beamwidth increases when it is blurred onto the substrate due to an increase in the distance laser-substrate, resulting in a denser weft of the different graphene strands induced by the laser beam due to the partial overlap of the laser spots (see Fig. 5). This phenomenon can be observed in Fig. 4, where two samples are shown with the beam focused (Fig. 4.a), and 2 mm out of the focus (Fig. 4.b). The results using this defocusing technique demonstrate a greater homogeneity of the graphene layer generated in the samples, as well as a higher conductivity, in agreement, respectively, with works [45] and [46]. Fig. 6 shows a reduction in sheet resistance up to 10-12 % for a 2 mm beam blur for samples with a laser power of 6.8 W and a scan speed of 120 mm/s. In addition, it has been observed that deviations from the average value depend on the laser cutting machine, on the calibration of the laser height relative to the surface, and in particular for small defocus heights. The motion resolution and repeatability of the machine also affect the number of track passes, contributing to variations in the sheet resistance. The impact of defocusing on the sheet resistance decreases when higher dots per inch (dpi) values are used.

2) ELECTROPLATING

Electroplating is a process that uses electrical current to reduce dissolved metal cations so that they form a coherent metal coating on an electrode. It is widely used in several industries to enhance the properties of metal objects, such as improving corrosion resistance, reducing friction, enhancing aesthetic appearance, and increasing thickness for undersized parts [47], [48]. The object to be plated (cathode) and a piece of the plating metal (anode) are immersed in the electrolyte solution. The cathode is connected to the negative terminal of a power supply, and the anode is connected to the positive terminal. When an electric current is passed through the electrolyte, metal ions from the solution are reduced and deposited onto the cathode. Simultaneously, metal atoms

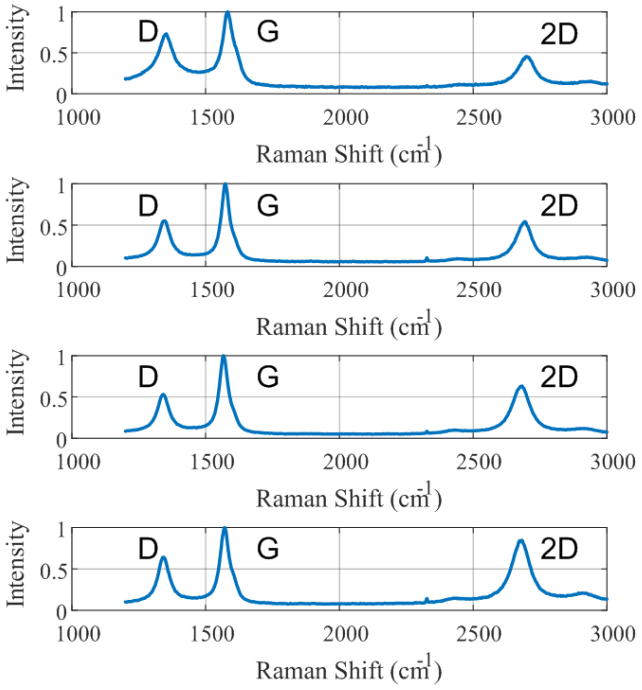

FIGURE 2. Raman spectra (a) Sample 1, (b) Sample 2, (c) Sample 3, and (d) Sample 4 (see Table 1 for the laser parameters used in each configuration).

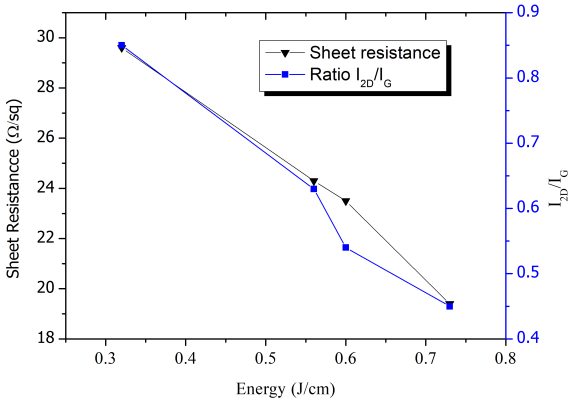

FIGURE 3. Sheet resistance (left axis) and 2D-to-G ratio of the Raman spectrum (right axis) as a function of the energy per unit length.

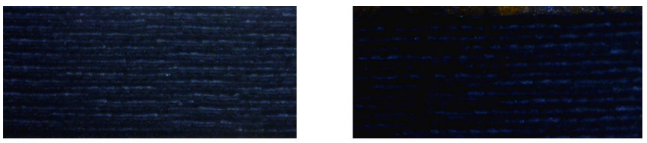

FIGURE 4. LIG samples obtained with a laser power of 6.8 W and a scanning speed of 200 mm/s (a) with the laser-focused and (b) with a 2 mm beam defocusing.

from the anode dissolve into the electrolyte, maintaining the concentration of metal ions in the solution. After the desired thickness of the metal coating is achieved, the object is removed from the electrolyte bath, rinsed, and dried. The thickness (t_p) of the electroplated layer can be calculated

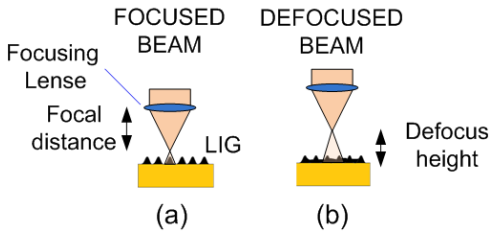

FIGURE 5. Effect of beam defocusing on the substrate. (a) Focused, (b) Defocused. The larger spot when the beam is defocused produces an overlap between traces.

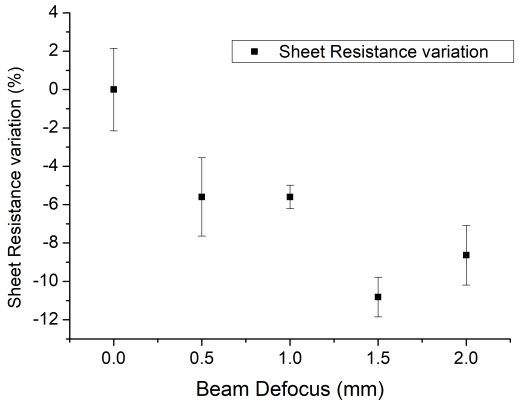

FIGURE 6. Normalized variation of sheet resistance as a function of laser beam defocusing (in mm), relative to the value when it is focused.

TABLE 1. Laser parameters employed.

Sample	Power (W)	Scan Speed (mm/s)	Energy (J/cm)	R_S (Ω/sq)	I_D/I_G	I_{2D}/I_G
1	8.8	120	0.73	19.4	0.73	0.45
2	7.2	120	0.60	23.5	0.55	0.54
3	8.4	150	0.56	24.3	0.53	0.63
4	6.4	200	0.32	29.6	0.64	0.85

using the formula derived from Faraday's law [49]:

$$t_p = \frac{I \cdot T \cdot M}{n \cdot F \cdot \rho_m \cdot A} \tag{1}$$

where I is the electrical current, T is the electroplating time, M is the molar mass of the plating metal (in grams per mole, g/mol), n is the number of electrons involved in the electrochemical reaction (valence number), F is the Faraday's constant (96485 C/mol), ρ_m the mass density of the plating metal (8.90 g/m^3 for Nickel), and A is the area of the electrode being plated. Nickel is a suitable metal for electroplating due to its unique properties and the benefits it imparts to plated objects. Nickel provides excellent protection against corrosion, making it ideal for use in harsh environments. Nickel forms strong bonds with various base materials, ensuring a uniform and durable coating. While it is not as conductive as copper or silver, nickel's conductivity is sufficient for many electrical applications, especially when combined with its corrosion resistance [50]. The cathode is the electrode where nickel's oxidation and deposition occur. The parts that have been previously patterned with LIG are connected to the cathode and a bar of nickel rod is used

as anode. The electrolyte is a salt of nickel, which in this work is the nickel-plating solution from Tifoo (Regensburg, Germany) that contains nickel sulfate. A current between 20 mA and 40 mA is typically used for the electroplating, which is driven from a DC power source (model Agilent E3632A) configured as a current source (limiting the current level). The thickness of the electroplated metal is a function of the time. The deposition is not uniform, which in this application gives another degree of randomness. The part of graphene that is in contact with the electrode is not electroplated and presents a high resistance, therefore, the electroplating procedure is repeated connecting the electrode in different locations. Since the conductivity of Laser-induced porous graphene is not very high (reported values are in the order of 200-2500 S/m [31]), the effective conductivity of the resonators is predominated by the high conductivity of the nickel ($1.43 \cdot 10^7$ S/m). In case it was necessary, the layer of Nickel could be used as a precursor or adhesion layer for electroplating other metals such as Au or Cu.

To investigate the effect of defects or nonuniformities of electroplating, a simple ring resonator is manufactured (width of 1 mm and radius of 10 mm) on the polyimide Kapton Dupont flexible substrate. The Kapton substrate has been attached with glue to a board of acrylic plastic of 300 μm height used as a support to avoid that the Kapton shrivels due to the heat. A laser power of 6.4W is used with scan rate of 200 mm/s to manufacture the LIG. The sheet resistance is obtained by measuring the DC resistance with two DC probes connected to a multimeter. Figure 7 shows the measured sheet resistance as a function of the electroplating time for two currents (20 mA and 40 mA). To better analyze the behavior, the inverse of the sheet resistance is represented ($1/R_{sq} = \sigma \cdot t$) being σ the effective or average conductivity of the sample, and t the total thickness of LIG plus the electroplated metal layer (nickel). The LIG is composed of parallel graphene threads where the laser beam has hit (see Fig. 8.a). Equation (1) predicts a linear relationship between the electroplated layer thickness and time. Consequently, the inverse of the sheet resistance is also linear assuming a constant value of the conductivity. However, the measured Raman spectrum reveals a porous graphene morphology. The figure shows two regions, each with a different slope. Nickel begins to permeate the porous interior of the graphene and progressively covers the entire surface (Fig. 8.b). When the nickel coats the surface (Fig. 8.c), the thickness of the nickel begins to increase, and consequently, the sheet resistance decreases faster. According to (1), the slope depends on the electroplating current. Note that in the second part, the current can be increased to reduce the electroplating time because the resistance of the conductor is enough to avoid applying high voltage to the samples that can produce undesired effects as the electrolysis of the solution. The skin depth is the measure of the penetration of an electromagnetic field inside a conductor [51]. Since it is inversely proportional to frequency, at high frequencies the field is concentrated in the surface, and consequently, the increase in resistance and

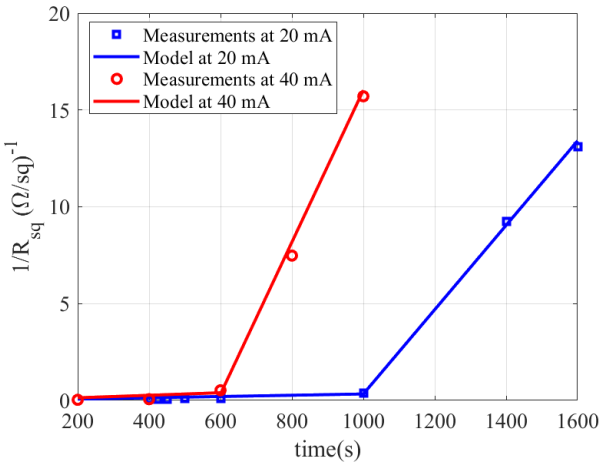

FIGURE 7. Comparison of the measured and the modeled inverse of the sheet resistance as a function of the electroplating time considering two different values of current.

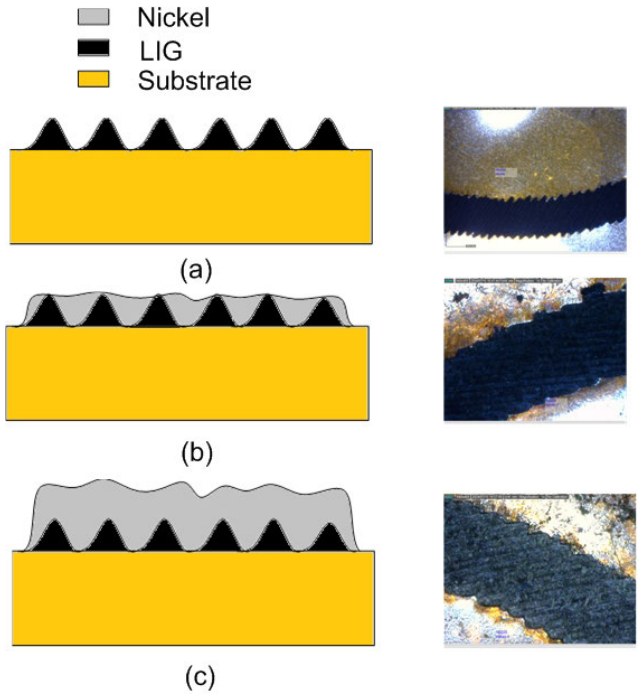

FIGURE 8. LIG surface cross-section and subsequent metallization by electroplating: (a) LIG surface is composed of parallel threads of graphene, (b) nickel penetration into graphene at the beginning of the electroplating process and (c) growth of the nickel layer as electroplating proceeds. A photography of LIG samples is shown on the right for each case.

losses are higher than in DC. The skin depth can be computed as:

$$\delta_c = \frac{1}{\sqrt{\pi \sigma f \mu_0}} \tag{2}$$

where σ is the conductivity, μ_0 is the magnetic permeability constant ($4\pi \cdot 10^{-7} H/m$) and f is the frequency. The resistance per unit length R can be approximated by [51]:

$$R = R_{DC} \frac{t}{\delta_c (1 - e^{-t/\delta_c})} \cdot \frac{1}{1 + t/W} \tag{3}$$

TABLE 2. Electroplating time at 20 mA, sheet resistance and quality factor of the measured resonators.

Sample	Electroplating Time(s)	Sheet Resistance (Ω/sq)	Quality factor
1	600	19.73	1.47
2	800	10.12	1.91
3	1000	2.54	6.0
4	1200	1.91	16.65
5	1400	0.11	19.18
6	1600	0.063	22.76

where R_{DC} is the resistance per unit length at DC (f = 0):

$$R_{DC} = \frac{1}{\sigma W t} \tag{4}$$

Finally, the quality factor associated with the conductor is obtained from [52] and [53]:

$$Q_c = \frac{\beta}{2\alpha_c} \tag{5}$$

where β is the propagation constant in the transmission line, Z_c is its characteristic impedance and α_c is the attenuation constant in Np/m associated to the conductor [52], [53]:

$$\alpha_c = R/(2Z_c)) \tag{6}$$

The overall quality factor (Q) is the combination of the quality factor due to the losses associated with the dielectric and the conductor [52], [53]:

$$1/Q = 1/Q_c + 1/Q_d \tag{7}$$

The quality factor associated to the dielectric can be obtained as:

$$Q_d = \beta/(2\alpha_d) \approx 1/tan\delta \tag{8}$$

where α_d is the attenuation constant in Np/m associated to the dielectric and $tan\delta$ is the dielectric dissipation losses. As will be seen experimentally, the quality factor values obtained with graphene-based resonators are low, so the predominant quality factor is that of the conductor.

III. RESULTS

A. CHARACTERISATION OF RESONATORS

The response of the resonator (parameter S_{21}) is measured with a VNA. Two microstrip lines printed on a 16 mil thick Rogers 4003 substrate are used to excite the six manufactured resonators shown (Fig. 9). These resonators have equal dimensions but different sheet resistances since the electroplating times are different. Each time the gray intensity is lighter it means that the thickness of the nickel layer increases and, therefore, the resistance of the sheet decreases. Table 2 lists the electroplating time used for each resonator and sheet resistance. The measurement setup shown in Fig. 10, and Figure 11 shows the S_{21} parameters measured from the six manufactured resonators. The measured quality factor as a function of the inverse of the sheet resistance is shown in Fig. 12. It is obtained by fitting the S_{21} response to a Lorentzian function using Matlab optimization toolbox [54], [55]. Table 2 shows the quality factor obtained for each measured resonator.

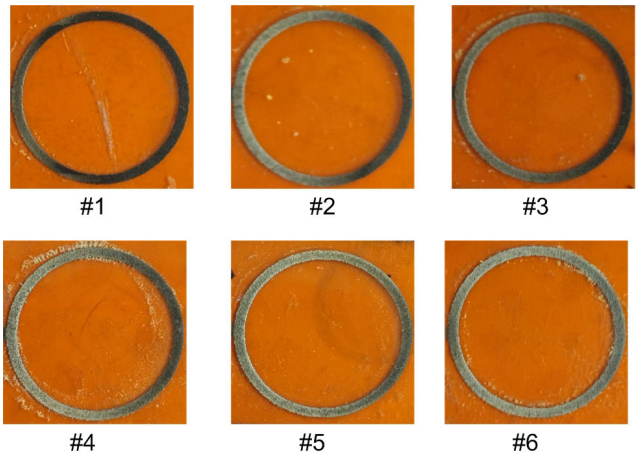

FIGURE 9. Photographs of the LIG annular resonator for different metallization thicknesses.

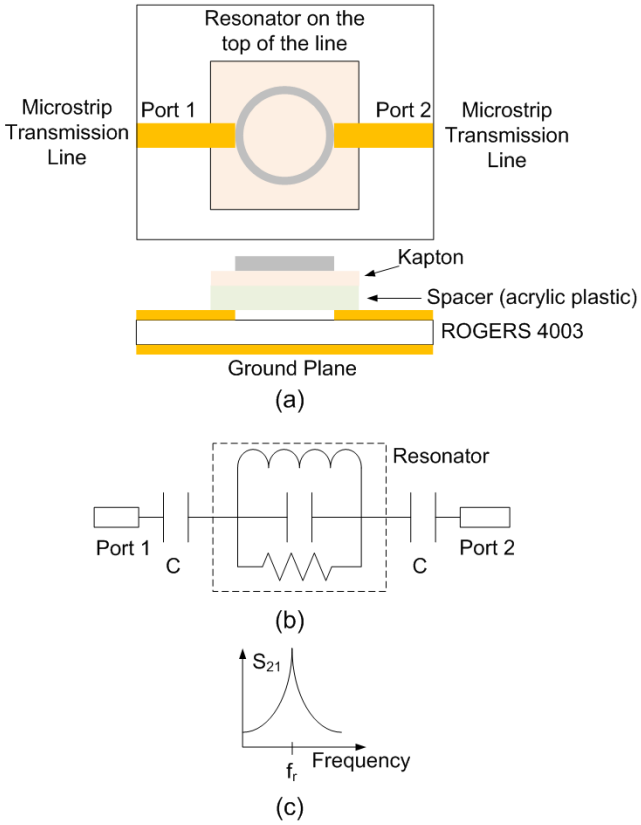

FIGURE 10. (a) Experimental setup used to measure the (S_{21}) parameter of the manufactured resonator (top view and transversal cut), (b) Equivalent circuit, where the electrical coupling is modeled as a parasitic capacitance, (c) Schematic of the frequency response. A maximum in the response of S_{21} is observed, coinciding with the resonant frequency f_r.

Fig. 13 shows the comparison between the measured and modeled quality factors as a function of the electroplating time (t_p). The modeled quality factor is obtained from the expressions (1)–(8). An effective conductivity that depends on the electroplated metal thickness (t_p) is considered,

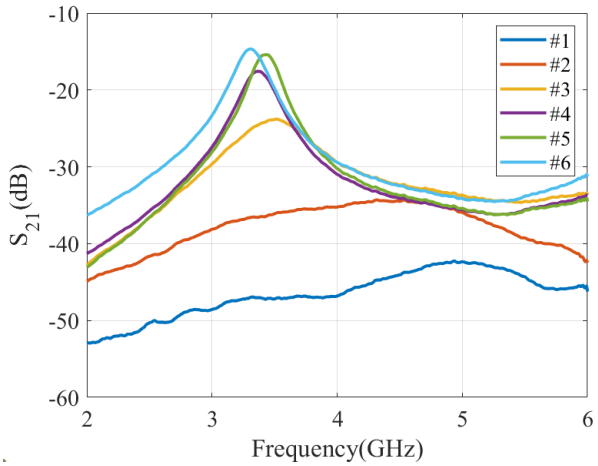

FIGURE 11. Measured transmission coefficient (S_{21}) as a function of the frequency of the ring resonators depending on the sheet resistance (see Table 2).

in order to take into account the lack of uniformity in the conductive layers. In Fig. 7, abrupt changes in the slope are observed when the metal thickness produced in electroplating is close to the thickness of the LIG. Therefore, the conductivity is modeled in two sections: the first one takes into account the average conductivity of the LIG, the metal immersed in this porous LIG, and the gaps between the traces; the second one considers the formation on the LIG of a rough layer of metal. Conductivity is modeled by the following expression:

$$\sigma(t_p) = \begin{cases} \dfrac{\sigma_{LIG} t_{LIG} + \sigma_1 \cdot t_p}{t_{LIG}}, & t_p \leq t_{LIG} \\ \dfrac{\sigma(t_{LIG}) t_{LIG} + \sigma_2 \cdot (t_p - t_{LIG})}{t_p}, & t_p > t_{LIG} \end{cases} \tag{9}$$

where t_{LIG} is the thickness of the LIG, which is 25 μm, σ_{LIG} is the conductivity of the LIG, whose estimated value of 2500 S/m is obtained from the DC sheet resistance, σ_1 and σ_2 are the conductivities of the electroplated metal within and on the LIG, respectively, and are considered fitting parameters. The values found are $\sigma_1 = 1.8 \cdot 10^4$ S/m and $\sigma_2 = 10^6$ S/m, which are lower than bulk nickel conductivity of due to the porosity and roughness, respectively. The thickness t_p is obtained from the electroplating time (1). Considering the proposed conductivity model, the measured and modeled results of the sheet resistance are in consonance themselves (see Fig. 7).

To calculate the quality factor, the same thicknesses of the metal (t) and the galvanized layer (t_p) are considered, because the fields are assumed to be concentrated on the surface of the most conductive metal. Good agreement has been obtained between the modeled and measured quality factor as a function of the inverse of sheet DC resistance (Fig. 12). Consequently, accurate and reliable estimation of RF parameters can be achieved from the parameter-based conductivity model derived from DC measurements. To monitor the manufacturing process, simple planar structures such as ring resonators or small strips can be used.

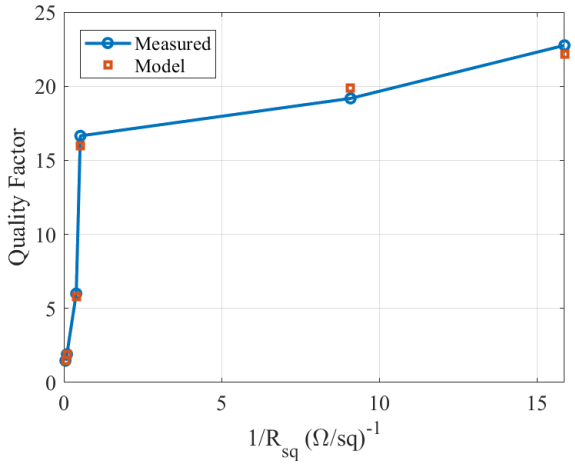

FIGURE 12. Measured and simulated quality factor of ring resonators as a function of the inverse of the sheet resistance.

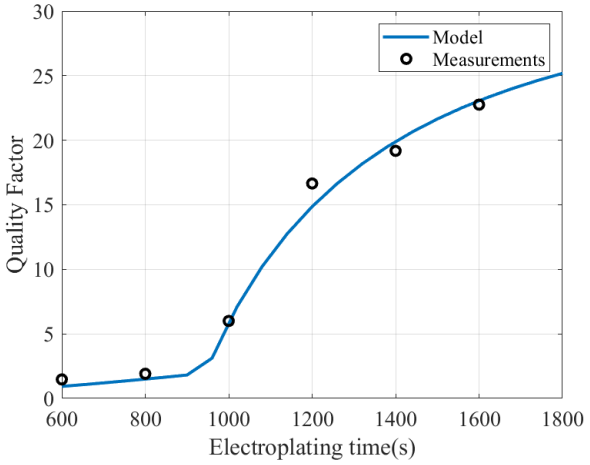

FIGURE 13. Modeled and measured quality factors as a function of electroplating time.

The root mean square (RMS) error between the measured S_{21} parameter, in dB, of two resonators i and j ($E(i,j)$) can be computed using the following expression:

$$E(i,j) = \sqrt{\frac{1}{N} \sum_{n=1}^{n=N} |20log(|S_{21i}(n)|) - 20log(|S_{21k}(n)|)|^2} \tag{10}$$

where N is the number of measured frequencies. Table 3 shows the computed error between pairs of resonators of Fig. 11. The standard deviation between 10 samples is found to be less than 0.1 dB, much lower than the mean error differences. Therefore, by modifying the electroplating time, the quality factor of the resonators can be adjusted, and consequently, although they are geometrically identical resonators and have similar resonance frequencies, they are

sufficiently different to be able to differentiate them from each other.

TABLE 3. Root mean square error E(i,j) (*dB*) between resonators.

Resonator Number	1	2	3	4	5	6
1	0	7.7	12.6	13.7	13.4	16.4
2	7.7	0	5.4	7.0	6.6	9.5
3	12.6	5.4	0	3.7	2.1	6.0
4	13.7	7.0	3.7	0	3.3	3.3
5	13.4	6.6	2.1	3.3	0	5.8
6	16.4	9.5	6.0	3.3	5.8	0

B. TAGS BASED ON COMPLEX ELECTROMAGNETIC SIGNATURES

Tags based on both geometry variations and variable conductance materials can be used as authentication tags. Due to its complexity, it is not possible to predict their spectral response, becoming a tag with complex signature [9]. What initially seems like a disadvantage is beneficial because the tags cannot be easily reproduced, especially if they are hidden inside the product or are covered with adhesive paper or dielectric material (eg. an opaque PET plastic). If this coating is removed, the metal tracks deteriorate, altering the tag's response.

The spectral response of this type of tags, characterized by their resonances, strongly depends on the position of the probe with respect to the metal parts that form it, unlike the classic resonator, in which the shape is well-defined and can be precisely placed close to the probe. Therefore, a mechanic scanner is developed to characterize the tags with complex signatures. It consists of a mobile platform where the probe, that is the microstrip transmission line, can be moved under the tag using a linear actuator controlled by a stepper motor. A 75μm Kapton spacer attached to two brackets separates the probe from the sample. The tag is attached to the spacer with adhesive tape. The microstrip line is connected to a VNA, which measures the parameter S_{21} for each position. Only the module of S_{21} is used, therefore a scalar system (eg. spectrum analyzer with tracking generator) could also be used to reduce the cost of the system. A top-view schematic and a photography of the experimental setup are shown in Fig. 14 and Fig. 15, respectively. In this work, the frequency range between 100 MHz and 10 GHz is used, which allows the measurement of the first resonance and sometimes the second one. The number of measurement frequency points is 1601 and the step between two consecutive positions is set to 0.5 mm.

To understand the working operation, some electromagnetic simulations of simple resonators are done. Three resonators have been considered (see Fig. 16). An equivalent circuit (Fig. 16) can be used to understand the simulations. The mutual coupling coefficient is a function of the distance. Therefore, only the resonances associated with the resonators close to the line (and their harmonics) can be detected in the measurements. As long as the resonator is far from the line (e.g., 5 mm in simulations), the minimum peak cannot be detected in the simulation. The resonance frequency depends on the length of the strip and can be easily adjusted by changing the layout. The resonators considered in this

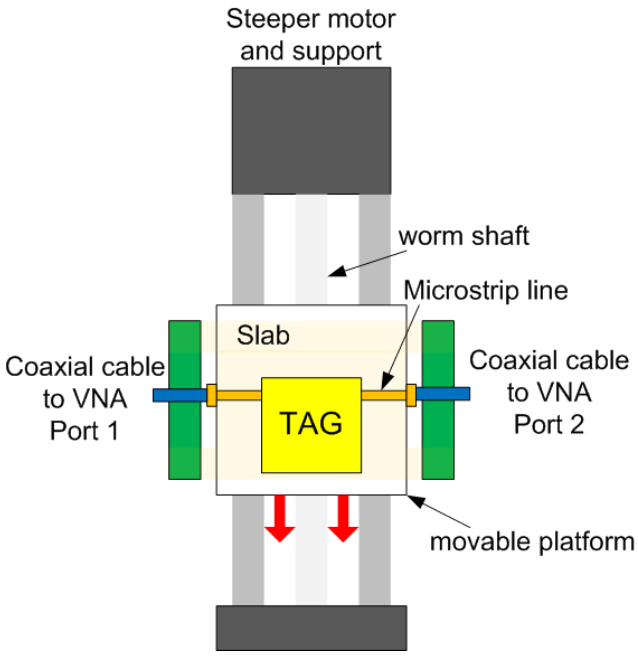

FIGURE 14. Schematic of the designed scanner to measure the spectra signature of complex tags.

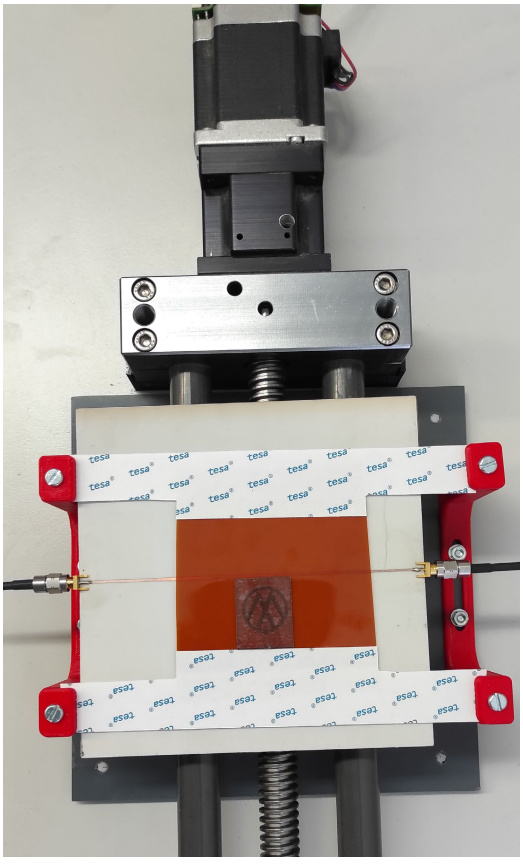

FIGURE 15. Phototgraphy of the scanner.

example have a square spiral shape of 7, 6, and 5 mm on a side. The number of turns of the strips is 3 and both their width and the spacing between them is 0.5 mm. The first resonance frequencies are 2.18 GHz, 2.85 GHz and 4.77 GHz, respectively. The substrate and metal chosen for the simulations are, respectively, 75 μm-thick Kapton and 17 μm thick nickel. The probe microstrip lines are patterned on a 16 mil-thick Rogers 4003 substrate and have a characteristic impedance of 50 Ω. Simulations are performed using Keysight's Momentum. Figure 17 shows the layout of the spiral resonators simulated at different distances from the edge of the microstrip line Figure 18 shows the simulated results for various positions of the resonators with respect to the microstrip line of the scanner. The absorption depth at multiple resonance frequencies depends on the quality factor of the resonators and can be adjusted by modifying the conductivity of the LIG-nickel compound. This example shows that simple multibit near-field tags can be designed. The number of bit combinations can be increased by increasing the number of resonators and the position of these resonators with respect to the microstrip line. Both coupling methods (magnetic and electrical) can be exploited to design tags. Magnetic coupling is more intense between parallel lines as in the last example. Electrical coupling is due to parasitic capacitances between strips as in the case of measurements of ring resonators. A multibit chipless tag based on U-shaped resonators has been proposed in [56] but using the same distance between the transition line and the resonators. However, in this type of multibit tag, the resonators are easily identifiable. Although cloning could be attempted by replicating the design, the challenge would be considerable, especially if a variable conductance such as the one proposed in this work is used.

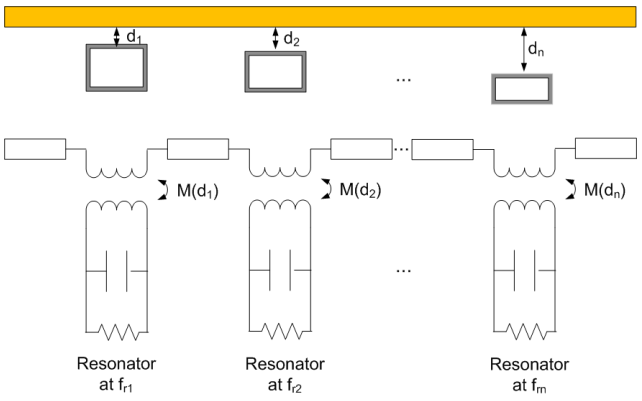

FIGURE 16. Multibit equivalent circuit.

To increase the complexity of electromagnetic signature, it is possible to embed resonators in images or to exploit the resonances produced by the shapes printed on them. Company logos made of LIG and subsequently electroplated can be used as authentication tags. To remove the losses of the line and better distinguish the resonance, the measured response for the first position (where the tags have nothing

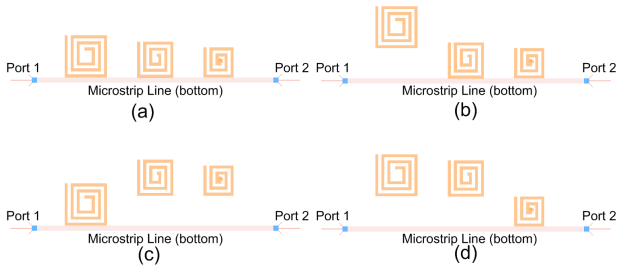

FIGURE 17. Layout of the simulated multibit resonators.

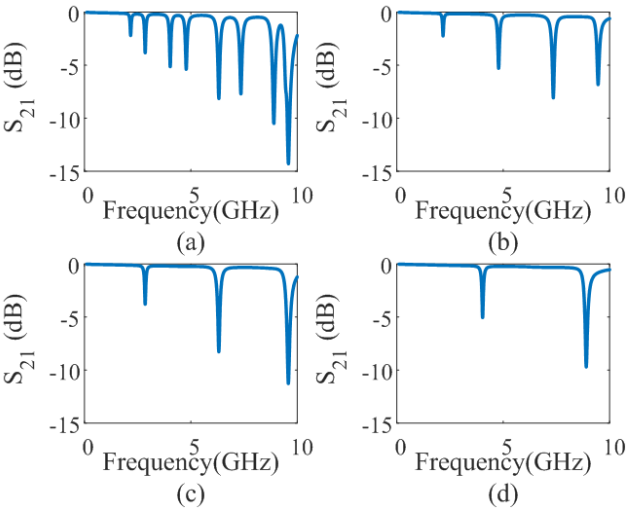

FIGURE 18. Simulation of parameter S_{21} as a function of the frequency for the following states: (a) 111, (b) 010, (c) 100, and (d) 001.

printed) is used as a reference and then subtracted from the responses at the other positions. Figure 20 shows an example of the uncorrected measurement corresponding to the Batman logo. Figure 19 shows the S_{21} parameter corresponding to the first position (0 mm), where one of the edges of the tag is aligned with the transmission line. A measurement example at the 3 mm position reveals the presence of resonances. After subtracting the reference, these resonances become more pronounced. The spectral signature (S_{21} parameter) after subtracting the reference measurement is shown in Fig. 21. Figures 21 through 24 show the measured spectral signatures of various logos or characters printed after the correction has been applied. The logos are manufactured with a laser power of 6.4 W, a scan speed of 200 mm/s, and an electroplating time of 1200 seconds at 20 mA.

By changing the shape, scale, relative position, laser parameters, electroplating time, or current, another tag with a distinguishable electromagnetic signature is obtained. Tags printed with complex shapes produce specific and unique bidimensional images that are quite difficult to be identified by visual inspection. Fig.25 shows the difference between two measurements of the same logo. Small differences can be attributed to VNA measurement errors. The VNA used in the experiments is Agilent PNA E8364C. The average absolute error obtained is only $1.47 \cdot 10^{-4}$ dB. To classify

the tags, the root mean square error of the spectral response as a function of the positions is used to sort the tags. The tag is identified if the RMS error is smaller than a threshold fixed at $3 \cdot 10^{-4}$ dB (two times the difference between the same tag) to take into account the uncertainty in the VNA measurement. The error is computed using (10), performing the average for all the positions and frequencies. For example, the error E(i,j) between the tags i and j shown in previous figures is listed in Table 4 showing that the tags are distinguishable between them.

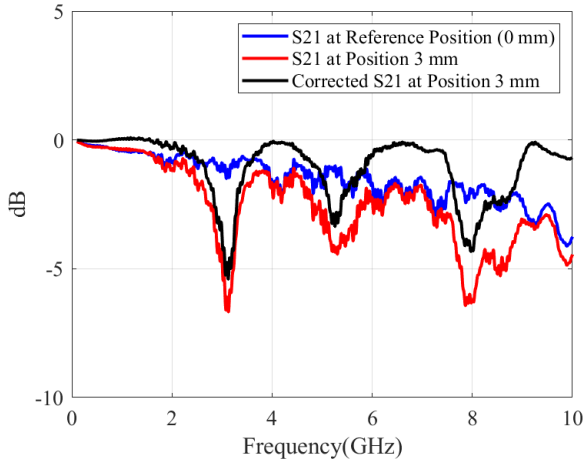

FIGURE 19. Measurement of the S_{21} parameter at the reference position (0 mm) and at 3 mm. The corrected S_{21} measurement is obtained by removing the estimated background from the reference position.

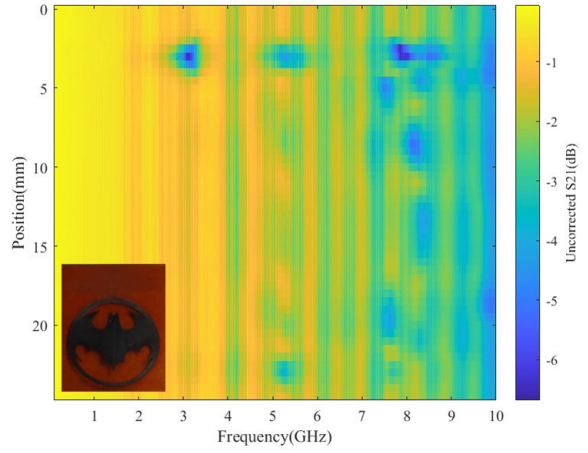

FIGURE 20. Measurement of the spectral response as a function of the position for the Batman's logo (see inset image). The uncorrected S_{21} parameter is shown without removing the losses of the transmission line.

To investigate the impact of misalignments, a series of measurements are conducted by intentionally changing the initial position with respect to the nominal one in order to simulate position errors when placing the tag on the scanner. Fig. 26 illustrates the Root Mean Square (RMS) error of one tag (Batman's logo) depending on its alignment. Additionally, the figure presents the RMS error between Batman and Toyota logos (the most similar alternative) as

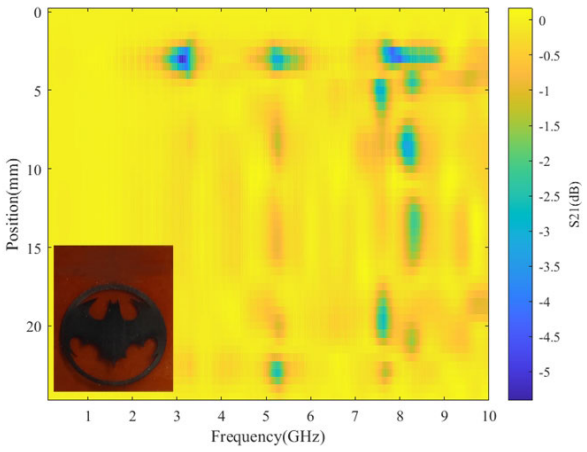

FIGURE 21. Measurement of the spectral response as a function of the position for the Batman's logo (see inset image).

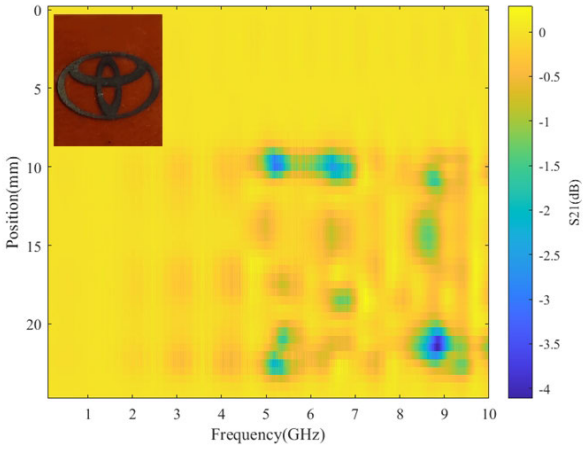

FIGURE 22. Measurement of the spectral response as a function of the position for the Toyotas's logo (see inset image).

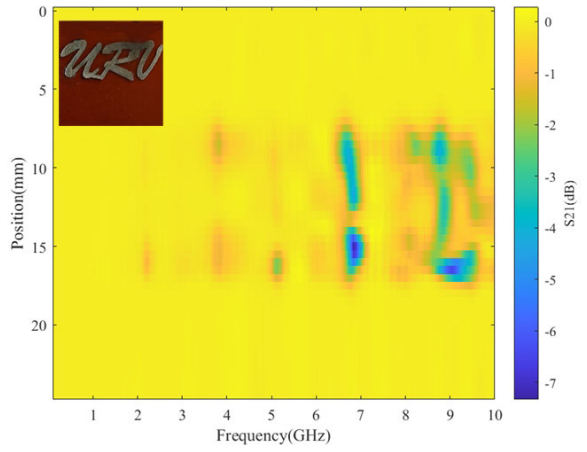

FIGURE 23. Measurement of the spectral response as a function of the position for some characters (see inset image).

a function of the misalignment in Batman's tag. The results show that the system tolerates misalignments typically up to $\pm$ 1.5 mm. This distance is approximately equal to the

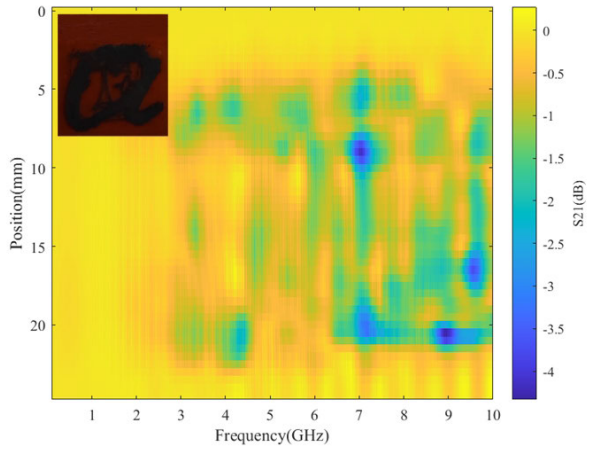

FIGURE 24. Measurement of the spectral response as a function of the position for the University Rovira i Virgili (URV) logo (see inset image).

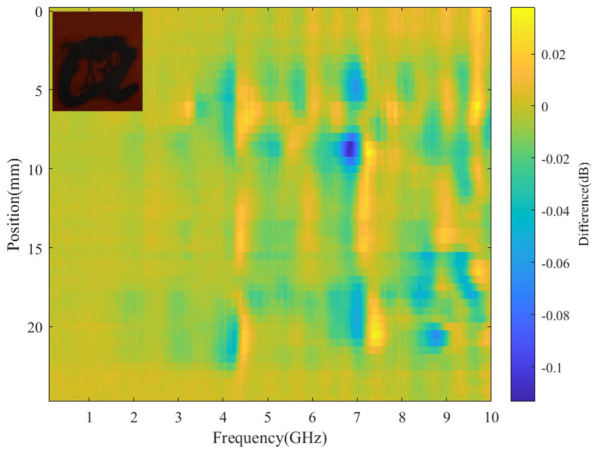

FIGURE 25. Difference between two measurements of the spectral response as a function of the position for the URV's logo (see inset image).

coupling distance between the resonator and the transmission line. When misalignment exceeds this distance, positions that previously excited the resonator and generated resonances no longer do so, causing a rapid increase in RMS error. In practice, the tag can be aligned with great precision using alignment marks or the edges of the tag itself. The combination of the stepper motor with micro-stepping and the linear actuator allows precise adjustment of the initial positioning and ensures high repeatability, as demonstrated in the results of Fig. 25.

TABLE 4. Root mean square error E(i,j) (*dB*) between tags of Fig. 21–24.

Tag	Fig. 21	Fig. 22	Fig. 23	Fig. 24
Fig. 21	0	0.53	0.74	0.71
Fig. 22	0.53	0	0.64	0.68
Fig. 23	0.74	0.64	0	0.76
Fig. 24	0.71	0.68	0.76	0

Due to the high resolution of the laser cutting machine (1000 dpi), small displacements can be introduced during the printing process to create tags with identical images or logos that generate distinct electromagnetic (EM) signatures. Figure 27 shows the average RMS error and standard deviation as a function of displacement of the logo measurements corresponding to Figs. 21–24 as a function of the shift distance. The RMS error increases rapidly, and tags can be clearly distinguished with an offset of the order of 0.5 mm.

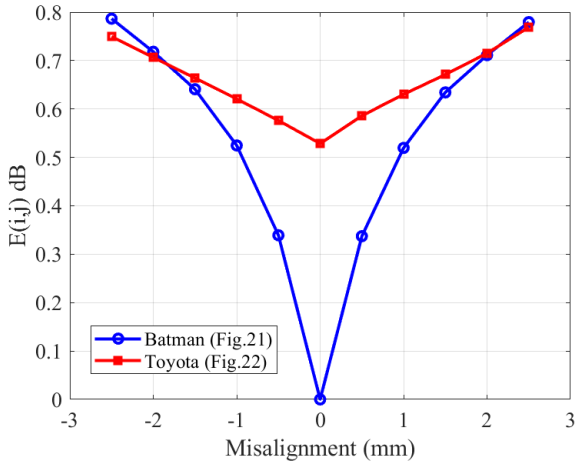

FIGURE 26. RMS error E(i,j) vs misalignment: Batman's tag (circles), and comparing batman and Toyota logos (squares).

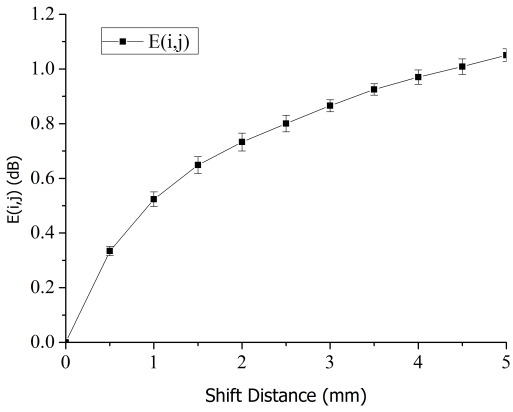

FIGURE 27. Average RMS error E(i,j) and standard deviation between two tags as a function of shifted distance.

IV. DISCUSSION

This section presents a comparison between the proposed solution and other previously published methods that are based on chipless RFID technology for authentication applications. The table 5 shows the references of the works related to the topic, the frequency bands used, and a brief description of each of them. The most common frequency band in most works is UWB, although the frequency depends on the design of the resonators. Some works are based on different forms of discrete resonators (dipoles in [22], C-shaped in [23], or circular ring slots in [24], whose resonant frequency can be modified by varying the dimensions of the resonator. Tolerance variations in the manufacturing

TABLE 5. Comparison of Chipless RFID technologies for authentication applications.

Ref.	Frequency Band (GHz)	Description
[22]	2-6	Resonance frequency of 3 dipoles over FR4 substrate
[25]	6.4	Reader composed by 4 × 4 PIFA antennas. Tag is random wires in a dielectric sealant
[24]	3-10	Concentric ring slots resonators
[27]	4	Circularly-shaped 40-bit encoder composed by slit ring resonators
[23]	10-16	C-folded quad-scatters tags
[26]	4-9	Embedded printed resonator in 3D printed tag
This work	0.1-10	LIG images and resonators

process introduce an additional degree of randomness that can be exploited in these types of applications [23]. The information of these chipless tags is obtained by using a VNA connected to two antennas in the far field to read the S_{21} parameter. Tag signature (e.g. resonance frequencies or backscattering response) is achieved after some signal processing to eliminate the clutter contribution associated with reflections from objects near the tag. The simplest processing method is to remove the background response of a previous measurement without including the tag and at the same distance [24]. There is another proposal that utilizes enhanced time-domain filtering techniques [23].

Another set of methods requires the use of a near-field reader, which eliminates the calibration challenges associated with far-field readout, assuming that read distance is not a critical factor for this application. In [26], flexible loop resonators have been embedded over a 3D-printed cylinder of PLA. A loop antenna connected to a VNA is used to read the resonance of the embedded loop in the near-field. In [27], a high-capacity chipless RFID system for security and authentication applications is introduced. The system utilizes a chain of split-ring resonators (SRRs) printed on a dielectric substrate, which are read in the near-field using another resonator, so that the frequency of the latter is detuned when approaching the SRR. Data encoding is achieved by the presence or absence of SRRs at predefined positions along the chain, and tag identification is based on sequential bit reading. A different approach has been proposed in [25], in which an unclonable tag is manufactured using metallic wires placed in random positions and fixed to a substrate with a dielectric sealant called RFDNA. The reader is composed of a matrix of antennas (4 × 4) designed at 6.4 GHz to maintain a small circuit size. All combinations of transmitter and receiver antennas are utilized to capture the electromagnetic signature or RF "fingerprint" of the tag.

In this work, the tag is based on an image (e.g. a logo) made with LIG, followed by an electroplating process to increase its conductivity. The cost of Kapton material is approximately 1.5 $\$/m^2$, making it not only more affordable than standard FR-4 PCB but also significantly more economical than typical substrates for RF applications, which are those used in most chipless tags, according to the work found in the literature. The use of Kapton flexible substrate allows the tag to be attached to bottles, product packaging, or labels for authentication certificates. Mass production can be achieved using industrial laser engraving machines, while electroplating is commonly applied in the manufacture of flexible circuits to protect traces from corrosion and improve component welding. Consequently, these industrial processes can be adapted to the proposed tag manufacturing. Therefore, the tags can be produced at low cost and in large quantities. Compared to conductive ink printing methods, no curing post-treatment is needed in this case, while the price of the tag is lower as the use of expensive conductive inks is avoided. It is possible to manufacture tags using conventional PCB fabrication techniques, such as using a thermal printer (e.g., printing an RFID tag with the Zebra printer). However, there is a loss in the degree of randomness associated with the variable conductance obtained with the combination of LIG and electroplating. Ultimately, this fact makes tags manufactured in the proposed manner significantly more difficult to clone than those made using conventional PCB manufacturing methods. The numerous fabrication parameters and geometric variations result in an unclonable tag with a unique electromagnetic signature. Moreover, a broadband scanner is proposed, which consists of a microstrip transmission line that scans the tag area. Thanks to the wide bandwidth, it is possible to capture more variations than those obtained in the case of working with a single frequency. On the other hand, the mechanical scanner provides more spatial information than that supplied by an array of discrete antennas as used in [25].

V. CONCLUSION AND FUTURE WORK

A method for the design of unclonable tags for anti-counterfeiting applications based on the measurement of electromagnetic spectral signatures in near-field has been proposed. The tags are composed of conductive shapes that present resonances at certain frequencies. The tags have been fabricated with laser-induced graphene (LIG) on polyimide and to obtain a variable conductivity an electroplating process has been carried out allowing to vary the quality factor of the resonators. The selection of the manufacturing parameters offers an additional level of security that can be added to the one provided by manufacturing imperfections against tag cloning. A two-dimensional scanner consisting of microstrip line that is moved under the tags has been presented. The measurement of the transmission coefficient is performed with a VNA in scalar mode (only magnitude information is used). The experimental results are highly promising, showcasing the feasibility of this technology for anti-fraud detection in brand protection.

REFERENCES

[1] F. Jordan and M. Kutter, "Identifying counterfeit medicines with industry-suitable technologies," *Pharmaceutical Eng., Offical Mag. ISPE*, vol. 32, no. 3, pp. 1–7, 2012.

[2] M. Kassab, J. DeFranco, T. Malas, P. Laplante, G. Destefanis, and V. V. G. Neto, "Exploring research in blockchain for healthcare and a roadmap for the future," *IEEE Trans. Emerg. Topics Comput.*, vol. 9, no. 4, pp. 1835–1852, Oct. 2021.

[3] Y. M. Al-Worafi, "Counterfeit medications in the developing countries," in *Handbook of Medical and Health Sciences in Developing Countries: Education, Practice, and Research*. Cham, Switzerland: Springer, 2023, pp. 1–20.

[4] J. P. Kennedy, "Counterfeit products online," in *The Palgrave Handbook of International Cybercrime and Cyberdeviance*. Cham, Switzerland: Springer, 2020, pp. 1001–1024.

[5] B. Lecat, J. Brouard, and C. Chapuis, "Fraud and counterfeit wines in France: An overview and perspectives," *Brit. Food J.*, vol. 119, no. 1, pp. 84–104, Jan. 2017.

[6] H. Yan and H. W. Siesler, "Identification of textiles by handheld near infrared spectroscopy: Protecting customers against product counterfeiting," *J. Near Infr. Spectrosc.*, vol. 26, no. 5, pp. 311–321, Oct. 2018.

[7] F. Saad, A. Baffoun, B. Mahltig, and M. Hamdaoui, "Polyester fabric with fluorescent properties using microwave technology for anti-counterfeiting applications," *J. Fluorescence*, vol. 32, no. 1, pp. 327–345, Jan. 2022.

[8] T. K. Agrawal, L. Koehl, and C. Campagne, "A secured tag for implementation of traceability in textile and clothing supply chain," *Int. J. Adv. Manuf. Technol.*, vol. 99, nos. 9–12, pp. 2563–2577, Dec. 2018.

[9] R. Pappu, B. Recht, J. Taylor, and N. Gershenfeld, "Physical one-way functions," *Science*, vol. 297, no. 5589, pp. 2026–2030, Sep. 2002.

[10] W. Yao, C.-H. Chu, and Z. Li, "The use of RFID in healthcare: Benefits and barriers," in *Proc. IEEE Int. Conf. RFID-Technol. Appl.*, Jun. 2010, pp. 128–134.

[11] S. C. G. Periaswamy, D. R. Thompson, and J. Di, "Fingerprinting RFID tags," *IEEE Trans. Dependable Secure Comput.*, vol. 8, no. 6, pp. 938–943, Nov. 2011.

[12] C. Bertoncini, K. Rudd, B. Nousain, and M. Hinders, "Wavelet fingerprinting of radio-frequency identification (RFID) tags," *IEEE Trans. Ind. Electron.*, vol. 59, no. 12, pp. 4843–4850, Dec. 2012.

[13] M. Kheir, H. Kreft, I. Hölken, and R. Knöchel, "On the physical robustness of RF on-chip nanostructured security," *J. Inf. Secur. Appl.*, vol. 19, nos. 4–5, pp. 301–307, Nov. 2014.

[14] L. Yang, P. Peng, F. Dang, C. Wang, X.-Y. Li, and Y. Liu, "Anti-counterfeiting via federated RFID tags' fingerprints and geometric relationships," in *Proc. IEEE Conf. Comput. Commun. (INFOCOM)*, May 2015, pp. 1966–1974.

[15] H. P. Romero, K. A. Remley, D. F. Williams, and C.-M. Wang, "Electromagnetic measurements for counterfeit detection of radio frequency identification cards," *IEEE Trans. Microw. Theory Techn.*, vol. 57, no. 5, pp. 1383–1387, May 2009.

[16] N. C. Karmakar, E. M. Amin, and J. K. Saha, *Chipless RFID Sensors*. Hoboken, NJ, USA: Wiley, 2016.

[17] D. Girbau, J. Lorenzo, A. Lazaro, C. Ferrater, and R. Villarino, "Frequency-coded chipless RFID tag based on dual-band resonators," *IEEE Antennas Wireless Propag. Lett.*, vol. 11, pp. 126–128, 2012.

[18] A. Lazaro, A. Ramos, D. Girbau, and R. Villarino, "Chipless UWB RFID tag detection using continuous wavelet transform," *IEEE Antennas Wireless Propag. Lett.*, vol. 10, pp. 520–523, 2011.

[19] A. Lázaro, R. Villarino, F. Costa, S. Genovesi, A. Gentile, L. Buoncristiani, and D. Girbau, "Chipless dielectric constant sensor for structural health testing," *IEEE Sensors J.*, vol. 18, no. 13, pp. 5576–5585, Jul. 2018.

[20] D. Girbau, Á. Ramos, A. Lazaro, S. Rima, and R. Villarino, "Passive wireless temperature sensor based on time-coded UWB chipless RFID tags," *IEEE Trans. Microw. Theory Techn.*, vol. 60, no. 11, pp. 3623–3632, Nov. 2012.

[21] M. Greene and G. W. Hurley, "Method for forming a radio frequency responsive target and apparatus for verifying the authenticity of same," U.S. Patent 6 471 878, Oct. 29, 2002.

[22] V. Deepu, A. Vena, E. Perret, and S. Tedjini, "New RF identification technology for secure applications," in *Proc. IEEE Int. Conf. RFID-Technol. Appl.*, Jun. 2010, pp. 159–163.

[23] Z. Ali, E. Perret, N. Barbot, R. Siragusa, D. Hély, M. Bernier, and F. Garet, "Detection of natural randomness by chipless RFID approach and its application to authentication," *IEEE Trans. Microw. Theory Techn.*, vol. 67, no. 9, pp. 3867–3881, Sep. 2019.

[24] K. Yang, D. Forte, and M. M. Tehranipoor, "UCR: An unclonable chipless RFID tag," in *Proc. IEEE Int. Symp. Hardw. Oriented Secur. Trust (HOST)*, May 2016, pp. 7–12.

[25] G. DeJean, V. Lakafosis, A. Traille, H. Lee, E. Gebara, M. Tentzeris, and D. Kirovski, "RFDNA: A wireless authentication system on flexible substrates," in *Proc. IEEE 61st Electron. Compon. Technol. Conf. (ECTC)*, May 2011, pp. 1332–1337.

[26] S. Genovesi, S. Choudhury, A. Gharibi, F. Costa, and G. Manara, "Additive manufacturing technologies for wireless anti-counterfeiting solutions," in *Proc. IEEE 13th Int. Conf. RFID Technol. Appl. (RFID-TA)*, Sep. 2023, pp. 130–133.

[27] C. Herrojo, J. Mata-Contreras, A. Núñez, F. Paredes, E. Ramon, and F. Martín, "Near-field chipless-RFID system with high data capacity for security and authentication applications," *IEEE Trans. Microw. Theory Techn.*, vol. 65, no. 12, pp. 5298–5308, Dec. 2017.

[28] X. Yu, H. Cheng, M. Zhang, Y. Zhao, L. Qu, and G. Shi, "Graphene-based smart materials," *Nature Rev. Mater.*, vol. 2, no. 9, pp. 1–13, Aug. 2017.

[29] A. Kaidarova and J. Kosel, "Physical sensors based on laser-induced graphene: A review," *IEEE Sensors J.*, vol. 21, no. 11, pp. 12426–12443, Jun. 2021.

[30] Z. Li, L. Huang, L. Cheng, W. Guo, and R. Ye, "Laser-induced graphene-based sensors in health monitoring: Progress, sensing mechanisms, and applications," *Small Methods*, 2024, Art. no. 2400118, doi: 10.1002/smtd.202400118.

[31] J. Lin, Z. Peng, Y. Liu, F. Ruiz-Zepeda, R. Ye, E. L. G. Samuel, M. J. Yacaman, B. I. Yakobson, and J. M. Tour, "Laser-induced porous graphene films from commercial polymers," *Nature Commun.*, vol. 5, no. 1, p. 5714, Dec. 2014.

[32] S. Madakam, R. Ramaswamy, and S. Tripathi, "Internet of Things (IoT): A literature review," *J. Comput. Commun.*, vol. 3, no. 5, pp. 164–173, 2015.

[33] S. Luo, P. T. Hoang, and T. Liu, "Direct laser writing for creating porous graphitic structures and their use for flexible and highly sensitive sensor and sensor arrays," *Carbon*, vol. 96, pp. 522–531, Jan. 2016.

[34] H. Cao, S. K. Thakar, M. L. Oseng, C. M. Nguyen, C. Jebali, A. B. Kouki, and J.-C. Chiao, "Development and characterization of a novel inter-digitated capacitive strain sensor for structural health monitoring," *IEEE Sensors J.*, vol. 15, no. 11, pp. 6542–6548, Nov. 2015.

[35] Z. Wan, N.-T. Nguyen, Y. Gao, and Q. Li, "Laser induced graphene for biosensors," *Sustain. Mater. Technol.*, vol. 25, Sep. 2020, Art. no. e00205.

[36] K. K. Adhikari, C. Wang, T. Qiang, and Q. Wu, "Polyimide-derived laser-induced porous graphene-incorporated microwave resonator for high-performance humidity sensing," *Appl. Phys. Exp.*, vol. 12, no. 10, Oct. 2019, Art. no. 106501.

[37] F. Salehnia, A. Lazaro, R. Villarino, M. Lazaro, N. Canyellas, X. Vilanova, E. Llobet, and D. Girbau, "Battery-free NFC sub-ppm gas sensor for distributed gas monitoring applications at room temperature," *IEEE J. Radio Freq. Identificat.*, vol. 7, pp. 630–643, 2023.

[38] A. Lamberti, M. Serrapede, G. Ferraro, M. Fontana, F. Perrucci, S. Bianco, A. Chiolerio, and S. Bocchini, "All-SPEEK flexible supercapacitor exploiting laser-induced graphenization," *2D Mater.*, vol. 4, no. 3, Jul. 2017, Art. no. 035012, doi: 10.1088/2053-1583/aa790e.

[39] X. Dai, J. Wu, Z. Qian, H. Wang, J. Jian, Y. Cao, M. H. Rummeli, Q. Yi, H. Liu, and G. Zou, "Ultra-smooth glassy graphene thin films for flexible transparent circuits," *Sci. Adv.*, vol. 2, no. 11, Nov. 2016, Art. no. e1601574. [Online]. Available: https://www.science.org/doi/abs/10.1126/sciadv.1601574

[40] A. Samouco, A. C. Marques, A. Pimentel, R. Martins, and E. Fortunato, "Laser-induced electrodes towards low-cost flexible UV ZnO sensors," *Flexible Printed Electron.*, vol. 3, no. 4, Dec. 2018, Art. no. 044002, doi: 10.1088/2058-8585/aaed77.

[41] T.-S. D. Le, S. Park, J. An, P. S. Lee, and Y.-J. Kim, "Ultrafast laser pulses enable one-step graphene patterning on woods and leaves for green electronics," *Adv. Funct. Mater.*, vol. 29, no. 33, Aug. 2019, Art. no. 1902771. [Online]. Available: https://onlinelibrary.wiley.com/doi/abs/10.1002/adfm.201902771

[42] R. Beams, L. G. Cançado, and L. Novotny, "Raman characterization of defects and dopants in graphene," *J. Phys., Condens. Matter*, vol. 27, no. 8, Mar. 2015, Art. no. 083002.

[43] A. M. Dimiev, G. Ceriotti, N. Behabtu, D. Zakhidov, M. Pasquali, R. Saito, and J. M. Tour, "Direct real-time monitoring of stage transitions in graphite intercalation compounds," *ACS Nano*, vol. 7, no. 3, pp. 2773–2780, Mar. 2013.

[44] J. C. Santos-Ceballos, F. Salehnia, A. Romero, and X. Vilanova, "Application of digital twins for simulation based tailoring of laser induced graphene," *Sci. Rep.*, vol. 14, no. 1, May 2024, Art. no. 10363.
[45] Y. Chyan, R. Ye, Y. Li, S. P. Singh, C. J. Arnusch, and J. M. Tour, "Laser-induced graphene by multiple lasing: Toward electronics on cloth, paper, and food," *ACS Nano*, vol. 12, no. 3, pp. 2176–2183, Mar. 2018.
[46] A. Mostaccio, G. Antonelli, M. Bragaglia, E. Martinelli, and G. Marrocco, "Comparative evaluation of laser induced graphene (LIG) traces on polyimide under soft and hard stress for IoT applications," *IEEE J. Flexible Electron.*, vol. 2, no. 3, pp. 256–264, May 2023.
[47] N. Kanani, *Electroplating: Basic Principles, Processes and Practice*. Amsterdam, The Netherlands: Elsevier, 2004.
[48] M. Schlesinger and M. Paunovic, *Modern Electroplating*. Hoboken, NJ, USA: Wiley, 2011.
[49] G. D. Wilcox and D. R. Gabe, "Faraday's laws of electrolysis," *Trans. IMF*, vol. 70, no. 2, pp. 93–94, Jan. 1992, doi: 10.1080/00202967.1992.11870951.
[50] J. Wang, D. R. Gabe, A. C. Hart, and P. C. Crouch, "The chemistry of nickel electroplating solutions," *Trans. IMF*, vol. 91, no. 1, pp. 4–10, Jan. 2013, doi: 10.1179/0020296712Z.00000000079.
[51] H. A. Wheeler, "Formulas for the skin effect," *Proc. IRE*, vol. 30, no. 9, pp. 412–424, Sep. 1942.
[52] D. M. Pozar, *Microwave Engineering: Theory and Techniques*. Singapore: Wiley, 2021.
[53] R. E. Collin, *Foundations for Microwave Engineering*. Hoboken, NJ, USA: Wiley, 2007.
[54] K. Leong, J. Mazierska, and J. Krupka, "Measurements of unloaded Q-factor of transmission mode dielectric resonators," in *IEEE MTT-S Int. Microw. Symp. Dig.*, vol. 3, Jun. 1997, pp. 1639–1642.
[55] P. J. Petersan and S. M. Anlage, "Measurement of resonant frequency and quality factor of microwave resonators: Comparison of methods," *J. Appl. Phys.*, vol. 84, no. 6, pp. 3392–3402, Sep. 1998.
[56] W.-S. Lee, H.-S. Jang, W.-S. Lee, K.-S. Oh, and J.-W. Yu, "Design of near-field chipless RFID tags and reader based on transmission line," in *Proc. Asia–Pacific Microw. Conf. (APMC)*, Nov. 2013, pp. 911–913.

ANTONIO LAZARO (Senior Member, IEEE) was born in Lleida, Spain, in 1971. He received the M.S. and Ph.D. degrees in telecommunication engineering from the Universitat Politècnica de Catalunya (UPC), Barcelona, Spain, in 1994 and 1998, respectively. He then joined as a Faculty Member with UPC, where he currently teaches a course on microwave circuits and antennas. Since July 2004, he has been a full-time Professor with the Department of Electronic Engineering, Universitat Rovira i Virgili (URV), Tarragona, Spain. His research interests include microwave device modeling, on-wafer noise measurements, monolithic microwave integrated circuits (MMICs), low phase noise oscillators, MEMS, RFID, UWB, and microwave systems.

MARCO RODRIGO CUJILEMA received the B.Sc. degree in electronic engineering and the M.Sc. degree in telecommunication engineering from the University of Calabria, Cosenza, Italy, in 2016 and 2019, respectively. He is currently pursuing the Ph.D. degree with the Department of Electronics, Rovira i Virgili University, Spain. He held positions as a contracted Professor with Universidad Tecnológica Equinoccial (UTE), from 2019 to 2022, and a Urban Operations Technician (OPU) with Telconet, from 2023 to 2024. His research interest includes laser-induced graphene (LIG).

FOAD SALEHNIA was born in Sanandaj, Iran. He received the Ph.D. degree in nanochemistry from the University of Tehran, in 2019. He subsequently pursued two postdoctoral positions with the University of Tehran. He is currently a Maria Zambrano Research Fellow with the MINOS Research Group, Universitat Rovira i Virgili, Tarragona, Spain. His research interests include synthesizing novel carbon-based nanomaterials and investigating their applications in sensing areas and energy conversion systems.

RAMON VILLARINO received the degree in telecommunications technical engineering from Ramon Llull University (URL), Barcelona, Spain, in 1994, and the degree in senior telecommunications engineering and the Ph.D. degree from the Universitat Politècnica de Catalunya (UPC), in Barcelona, in 2000 and in 2004, respectively. From 2005 to 2006, he was a Research Associate with the Technological Telecommunications Center of Catalonia (CTTC), Barcelona. He was a Researcher and an Assistant Professor with the Universitat Autònoma de Barcelona (UAB), from 2006 to 2008. Since January 2009, he has been a full-time Professor with Universitat Rovira i Virgili (URV), Tarragona, Spain. His research interests include radiometry, microwave devices, and systems based on UWB, RFIDs, and frequency selective structures using MetaMaterials (MM).

MARC LAZARO was born in Tarragona, Spain, in 1995. He received the B.S. degree in industrial electronics and automation engineering and the M.S. degree in electronic systems engineering and technology (METSE) from Rovira i Virgili University, Tarragona, in 2017 and 2018, respectively, where he is currently pursuing the Ph.D. degree with the Department of Electronics. Up until now, he has accumulated professional experience as a Data Acquisition Engineer and an Embedded Systems Developer. His research interests include semipassive RFID technologies based on backscattering communication and novel applications based on millimeter wave identification (MMID).

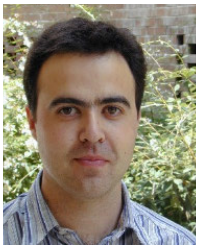

DAVID GIRBAU (Senior Member, IEEE) received the B.Sc. degree in telecommunication engineering, the master's degree in electronics engineering, and the Ph.D. degree in telecommunication from the Universitat Politècnica de Catalunya (UPC), Barcelona, Spain, in 1998, 2002, and 2006, respectively. From February 2001 to September 2007, he was a Research Assistant with UPC. From September 2005 to September 2007, he was a part-time Assistant Professor with the Universitat Autònoma de Barcelona (UAB). Since October 2007, he has been a full-time Professor with Universitat Rovira i Virgili (URV), Tarragona, Spain. His research interests include microwave devices and systems, with an emphasis on UWB, RFIDs, RF-MEMS, and wireless sensors.